A 2 Degree-of-Freedom SOI-MEMS Translation Stage With Closed-Loop Positioning

Bonjin Koo, Xuemeng Zhang, Jingyan Dong, Srinivasa M. Salapaka, and Placid M. Ferreira

Abstract—This paper presents the design, analysis, fabrication, and characterization of a closed-loop XY micropositioning stage. The stage design is based on a 2 degree-of-freedom parallel kinematic mechanism with linear characteristics. Integrated with sensing combs, and fabricated in SOI wafers, the design provides a promising pathway to closed-loop positioning microelectromechanical systems platform with applications in nanomanufacturing and metrology. The XY stage provides a motion range of 20 micrometers in each direction at the driving voltage of 100 V. The resonant frequency of the XY stage under ambient conditions is 600 Hz. The positioning loop is closed using a capacitance-to-voltage conversion IC and a feedback controller is used to control position with an uncertainty characterized by a standard distribution of 5.24 nm and a closed-loop bandwidth of about 30 Hz.   [2011-0149]

Index Terms—Closed-loop control, MEMS-scale nanopositioner, nanopositioning, parallel kinematic mechanism.

I. Introduction

PRECISE multi-axis positioning is critical to a number of micro- and nanomanipulation and probing technologies. Many applications such as fiber optical switches [1], micro-force sensors [2], [3], scanning probe microscopy [4], [5], data storage [6]–[8], [26], and microoptical lens scanner [9]–[12] depend on such precise positioning capabilities, and for these applications, size, motion range, natural frequency, and cross-coupling of motion along the different degrees of freedom are most important characteristics that are directly related to a system's performance. Microelectromechanical systems (MEMS)-scale positioning devices can play an important role in many of these situations. As primary positioning systems, they can reduce the overall system size or, as secondary positioning systems, they can provide a fine positioning/adjustment system very close to the functional element of the system and thereby 1) reduce stacked up of errors, 2) decrease vulnerability to environmental changes, and 3) improve bandwidth and dynamic performance.

Motivated by these applications and considerations, many MEMS-scale stages were introduced and developed. Previous research efforts in stage development [2], [3] have led to stages by directly connecting to two orthogonal combs to the moving table to generate X and Y displacement. Such designs result in very small workspaces and produce side instabilities due to the gap changes between comb fingers due to crosstalk between the two axes of motion. The widely used XY stage design [5], [6], [8], [10], [13]–[15] uses four identical comb actuators arranged around the end-effector, each perpendicular to its neighbor, and connected to it by long slender beams. When the stage is actuated in the X direction, the beam along the Y direction acts as a leaf spring to accommodate the motion of the X axis and vice versa. The crosstalk between the axes is decreased by reducing the stiffness of these beams. The net result, however, is nondeterminism in the motion produced (particularly when resisting forces are present) and an inability to arrest rotations. Further, the reduced stiffness leads to lower resonant frequencies and complex dynamics [16] with multiple modes in a fairly narrow frequency band. Serial kinematic linkage designs [11], [12] realize 2° of freedom by serial conjugation of single degree-of-freedom (DOF) systems. In these designs, one stage (called the inner stage) is embedded into the moving part of the other (outer) stage. The actuation of the outer stage moves the entire inner stage with the actuator of the inner stage producing a motion in a direction orthogonal to that produced by the outer stage. Thus, the end-effector, carried by the inner stage, can be moved in both, the X and Y, directions. Notwithstanding the difficulties of fabricating such a system and electrical isolation problems associated with electrical connections in the inner stage, an additional disadvantage of this design is that inertial load of the outer axis is significantly larger than of the inner axis, causing a decrease of the natural frequency and response time of the outer axis and mismatched dynamics between the two axes of motions.

Our research, therefore, has concentrated on adapting parallel kinematic systems, which have been widely used for macro- and mesoscale positioning systems [17]–[19], [23], to silicon-based MEMS-scale micropositioners. A parallel kinematic mechanism (PKM) consists of a fixed base and movable end-effector connected, in parallel, by multiple independent kinematic chains, each constraining the end-effector along one DOF while accommodating or admitting displacements along the other DOFs. Together, these chains restrict all undesired motions (for example, all rotations for a translational stage). In this way, a mechanism is realized in which the desired DOFs are spanned by the actuators and the undesired DOFs are restricted by the interaction of the kinematic chains. PKMs generally
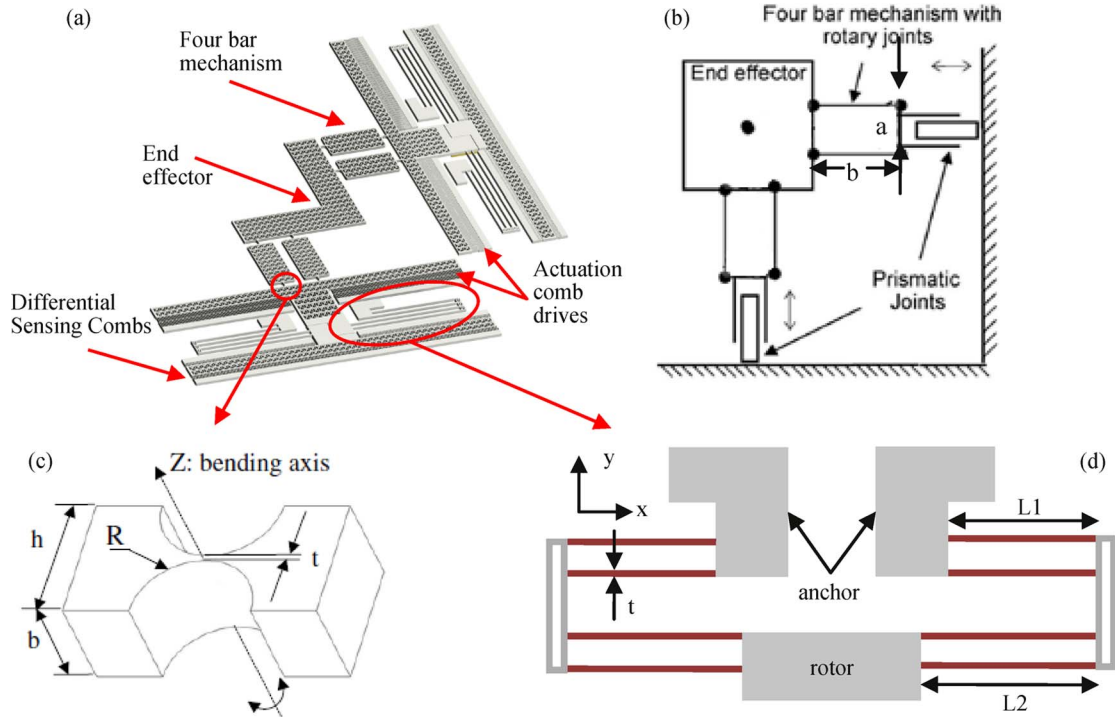
Fig. 1. Schematic diagram of XY micropositioning stage. (a) Solid model for XY micro stage. (b) Kinematic model for XY microstage. (c) Single-axis flexure hinge. (d) Leaf spring.

produce high structural stiffness because of their truss-like structures resulting in higher natural frequencies, and when appropriately designed, can result in configurations where near complete decoupling of the actuation is achieved. PKMs are criticized for the small workspaces or motion ranges because the motion is restricted to the intersection of the motion range of all its kinematics chains. While a valid criticism for macroscale systems, where the kinematic joints and actuators have large permissible motion ranges, for MEMS stage designs in which the motion range of the stage is more likely to be governed by the limits of the actuators and flexure joints than the mechanism itself, this is not an issue.

In the past, our work has introduced electrostatically driven, MEMS-scale, parallelogram four-bar stage designs and used both, linear and rotary combs to actuate them [20], [21], demonstrating decoupled XY motion of about 20 micrometers with stage bandwidths of about 1 kHz and Q-factors of about 100; three DOF stages with two translations and one rotation $(XY\theta)$; stages with tilt-plate actuated cantilevers for XY&Z motion [20]; and approaches to actuating and sensing on using a single comb structure [22]. These devices were all operated in open loop without any feedback signal on displacement, which was sufficient for applications that did not require precise positioning.

In this paper, motivated by applications such as tissue and cell testing in mechanobiology [24], [25] and scanning probe microscopy [5], we address the closed-loop control of the axes of the stages. Sensing combs, added to each axis of the stage, are designed to work with an inexpensive commercially-off-the-shelf capacitance-to-voltage conversion IC to realize closed-loop XY positioning stage with a sub-10-nm resolution. Section II summarizes the design of the stage for closed-loop

operations, while Section III provides an overview of the fabrication steps and the characterization of the sensing combs and the open loop behavior of the stage. Section IV describes the closed-loop performance of the system, and Section V draws up conclusions and recommendations for future work.

II. STAGE AND SYSTEM DESIGN

The basis of the stage design is a variation of a parallel-kinematic scheme [20] that has been successfully been adapted for MEMS-scale devices driven by linear electrostatic combs [20]–[22]. A solid model of the stage, along with its kinematic scheme is shown in Fig. 1. The end-effector or table is connected to the base by two kinematic chains, each consisting of freely mobile four-bar parallelogram linkage mechanisms carried by a controlled prismatic joint. The two prismatic joints provide the independent controlled displacements in the X and Y directions while the freely mobile four-bar system in each kinematic chain provides it with the degree of freedom to accommodate the controlled motion of the other. Kinematically, the table is the connector for the two four-bar linkages and, because of the parallelogram geometry of the four-bar mechanisms, it does not undergo any rotation. Thus, a 2 DOF, planar translator is obtained. For the MEMS-scale stage, the controlled prismatic joint is physically realized by a linear comb electrostatic drive mounted on a leaf spring, while the four-bar mechanism is realized by connecting rigid members by flexure hinges as shown in Fig. 1(a). The second pair of linear combs in the system is sensing combs designed to enable feedback control of the system. It is important to note that, for the range of motion desired in such MEMS-scale systems, these designs have been found to produce linear, decoupled, orthogonal motion.
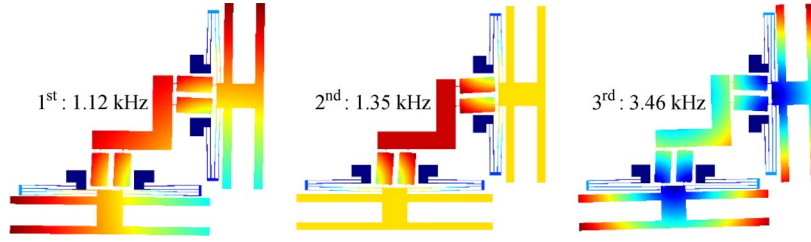
Fig. 2. Mechanical natural frequencies without damping condition and corresponding modal shapes in XY-plane.

Detailed kinematic and dynamic analyses as well as the rationale for designing components of the stage have been previously reported [20], [21]. Here, we use the same approaches and design and refer the reader to those references for additional details. The stage is designed for a fabrication on an SOI wafer, with a heavily doped 50 micrometer device layer, a 500-micrometer handle layer, and a 2-micrometer BOX layer. The leaf springs [design shown in Fig. 1(d)] have been designed with dimensions of $L1 = 1.38$ mm and $L2 = 1.90$ mm and leaf thickness of 8 μm, to obtain spring constants for the X direction and Y direction, i.e., kx and ky, is 1.85 N/m and ~83 000 N/m, respectively. Therefore, the ratio of two stiffness, ky/kx, is ~45 000. All rotational hinges [See Fig. 1(c)] are designed with thickness $t = 6$ μm, $R = 300$ μm, $h = 70$ μm, and $b = 50$ μm (refer Fig. 1), to produce a stiffness and maximum rotation range (based on the yield limit) of $3.1 \times 10\text{-}6$ N m rad-1 and 0.68 rad, respectively. The length of the parallelogram 4-bar links is 1 mm, thus allowing a maximum 630 μm displacement of the four-bar mechanism. Factors such as the maximum displacement of the comb drives predominantly determine the maximum displacement of each axis.

The actuation combs are designed with 188 fingers and 50 μm finger height (device layer thickness), 5 μm finger spacing, and 10 μm nominal overlap. They are designed to produce electrostatic force that is sufficient to overcome the resistance of folded spring and flexure hinges to produce the desired motion at a designed maximum actuation voltage. The electrostatic force, given by $F = n(\varepsilon_0 h V^2 / g)$, where n is the number of finger pairs $(= 188)$, h is the height of a finger (50 μm), g is the gap between two neighboring fingers (5 μm), and ε_0 is the electrical permittivity of air, is 81.5 μN at 70 V. This force, given the designed stiffness of the leaf and rotational springs and the kinematics of the mechanism, produces a displacement of 22 μm.

Modal analysis is performed by finite-element analysis (FEA) on the device to estimate its dynamic responses. Fig. 2 shows the results of this analysis, suggesting that the first two modes are pure translations along the (1, 1) and (−1, 1) directions (i.e., with the leaf springs in antiphase and in-phase deflection) with associated modal frequencies of 1.12 and 1.35 kHz. The next mode is a rotational mode with a modal frequency of 3.46 kHz and therefore around ten times stiffer than the translational modes.

Out-of-plane sagging of the stage due to its own weight can lead to the twisting of the leaf springs, misalignment between the comb fingers affect the orientation of the stage and introduce additional stresses at the hinges. A surface load corresponding to the weight of the structure is applied to the
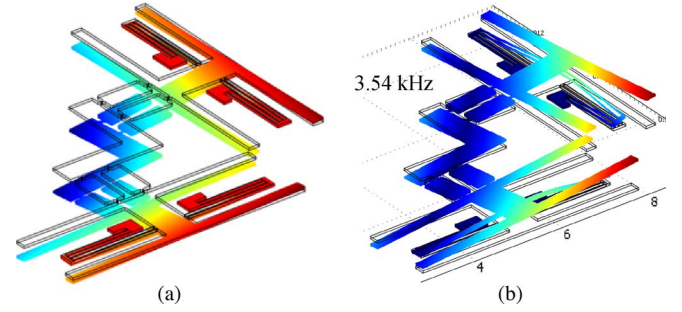

Fig. 3. (a) Maximum device deflection under self weight less than 20 nm. (b) Model shape and natural frequencies of the dominant Z-mode.

top surface of the device. FEA shows that the sagging effect of the stage under self-weight is negligible (less than 20 nm at the comb drives) when compared with the overall dimension of the device. From 3-D FEA, the dominant mode in z-direction is about 3.54 kHz, as shown in Fig. 3, The XY modes from 3-D analysis are similar to that from 2-D simulation. Since Z-mode is much stiffer than XY modes and actuation is along XY-axis, the out-of-plane motion is negligible for this device.

The stage has built-in differential capacitance sensing combs for each axis. They produce a capacitance change that is proportional to the displacement of the axis and sensed by a capacitance-to-voltage chip, the MS3110 Universal Capacitive Readout IC. The voltage generated by the IC is used as the feedback signal for the closed-loop control of the device. The chip has a resolution of 4.0 aF/$\sqrt{\text{Hz}}$ and a range up to 10 pF. The differential capacitance comb sensing system is made up of two opposed combs so that motion of the axis reduces the finger overlap (and hence, capacitance) for one comb while increasing that for the other. The first, SENS1 has 188 fingers, while the second, SENS2 has 156 fingers. Each finger has a height of 50 μm (the thickness of the SOI device layer) with a gap of 5 μm between the adjacent fingers. The initial overlap between the moving and stationary fingers for SENS1 and SENS2 are 30 μm and 10 μm, respectively. With an actuation voltage of 70 V, the finger overlaps of the two sensing combs change by 10 μm, corresponding to theoretical differential change in capacitance of 0.305 pF. Therefore, the sensing comb produces a capacitive change rate, $\Delta C / \Delta x$, of 0.0305 pF/μm with air being the medium between the comb fingers.

The device presented in this paper has an actuation comb and a differential sensing comb designed for each axis. The electrical isolation between the actuation comb drive and sensing comb drive is very important for the achievable performance of the closed-loop control. If the actuating combs and the sensing combs are electrically connected together, it will impose an
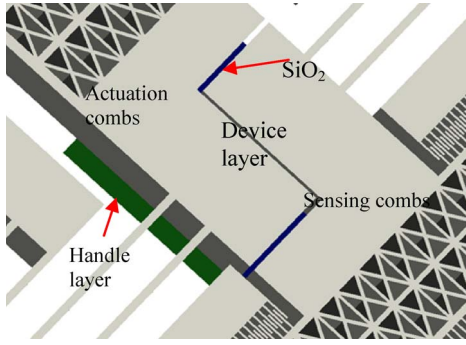
Fig. 4. Three-dimensional schematic model demonstrate the isolation of the for XY stage near isolated device layer.
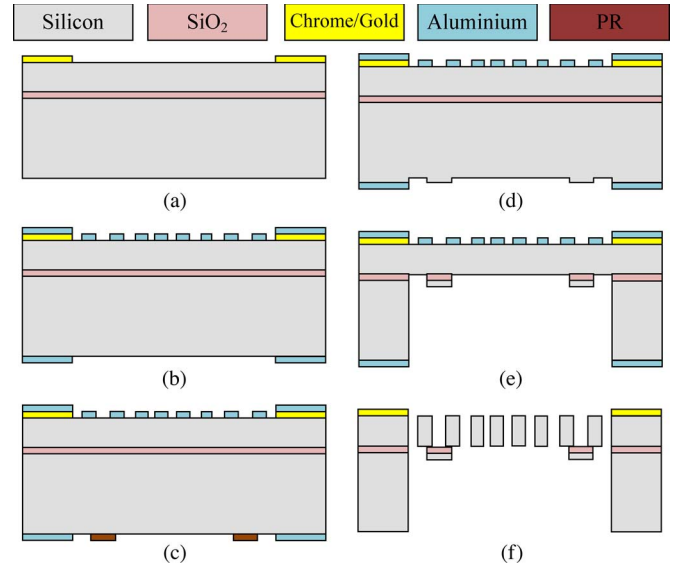

Fig. 5. Cross-sectional views for process flow. (a) Chrome/gold deposition to create electrodes to comb drive. (b) Top-side/bottom-side aluminium mask patterning. (c) PR retardation layer patterning. (d) DRIE of bottom-side silicon (create retardation layer). (e) Complete DRIE and HF etching to remove oxide layer. (f) DRIE of top-side silicon followed by aluminium mask etch.

impediment in circuit design since the actuator requires high actuation voltage (typically more than 50 V) while the sensing signal usually is less than 5 V. To reduce the interference between actuation and sensing circuits, in our device design, the sensing and the actuation combs are mechanically separated and electrically disconnected in the device layer, but are mechanically jointed together by an underlining connection pad that is composed of the insulation SiO_2 (buried oxide) layer and partially etched handle layer silicon, as shown in Fig. 4. The thickness of the handle layer silicon in the connection pad is controlled by etching retardation, so as to minimize the weight from the connection pad.

A dSPACE (DS1104) controller with analog voltage input/ output channels is used to receive the sensing displacement signal and provides the actuation command. The output of the sensor is fed into the dSPACE controller through a 16-bit D/A converter which has a resolution of 76.29 μV. With the MS3110 IC's resolution of 4.0 aF/$\sqrt{Hz}$, a theoretical capacitance sensing resolution and positioning resolution can be calculated, and they are 1.05E-5 pF and 0.64 nanometers, respectively.

III. FABRICATION AND CALIBRATION

The overall fabrication procedure for MEMS XY positioning stage is summarized in Fig. 5. The stage is fabricated in a SOI wafer with 50 μm of p-doped device layer and 500 μm handle in four photolithography patterning steps; two top-side patterning steps (one for patterning the actual device and one for the chrome/gold electrodes) and two bottom-side patterning steps (one for patterning handle layer cavity, and one for patterning connection pads with etching retardation). The retardation layer is a PR mask that is used to make mechanical connection ($\sim$70 μm thick) pad. During the long deep reactive ion etching (DRIE) process for etching the handle layer silicon, with the retardation PR, a 70 μm thick pad structure is left on the handle layer silicon.

During the fabrication, the gold/chrome electrodes are first patterned. Using the electrode features for alignment, the device pattern including the comb drives, folded spring, flexure hinges, and end effector are transferred to an aluminium film on the device layer of the die using standard lift-off processes. Next bottom-side patterns for cavity and retardation layer are transferred to handle layer in order, and DRIE is used to open up a large cavity below the device with 70 μm thick connector

shown in Fig. 4. This is followed by an HF (hydrofluoric) acid etch to remove the now-exposed buried oxide layer in the cavity. DRIE is repeated on the top-side to complete and release the device. Finally, the aluminium mask used for top-side and bottom-side patterns is etched away. Fig. 6 shows the results of the fabricated device.

The fabricated device performance is first checked with LCR meter (Agilent 4284A) to verify that a change of capacitance is detectable at the combs. For each axis of the stage, the capacitance of each sensing comb drive is recorded by the LCR meter while it is also being driven by a voltage bias, swept from −40 V to 40 V with step increases of 0.5 V. Fig. 7 shows data for five consecutive voltage sweep measurements on one of the sensing combs of the stage, indicating that a clearly measurable displacement signal is possible using the MS3110 chip. Additionally, notable information from LCR meter is that the initial parasitic capacitances associated with the combs is relatively high due to larger domains of doped silicon associated with the routing of contacts to the device and the relatively large test pads, leads, and probe contact. Because of small working capacitance range of MS3110 sensor, the sensing circuit is designed to work in a differential mode to accommodate this large parasitic capacitance.

The actuator combs are characterized by measuring the static displacement as a function of the driving voltage. To do this, each actuation comb is driven by a power supply (Keithley 237) and the displacement of the comb is observed by tracking a feature on the end-effector using a high-resolution (1-micrometer) optical microscope as the actuation voltage is increased in steps of 5 V to maximum of 100 V and then decreased by the same steps back to zero. Fig. 8 shows displacement as a function of diving voltage at the x and y axes actuation combs. The typical second-order voltage-displacement characteristics are observed.
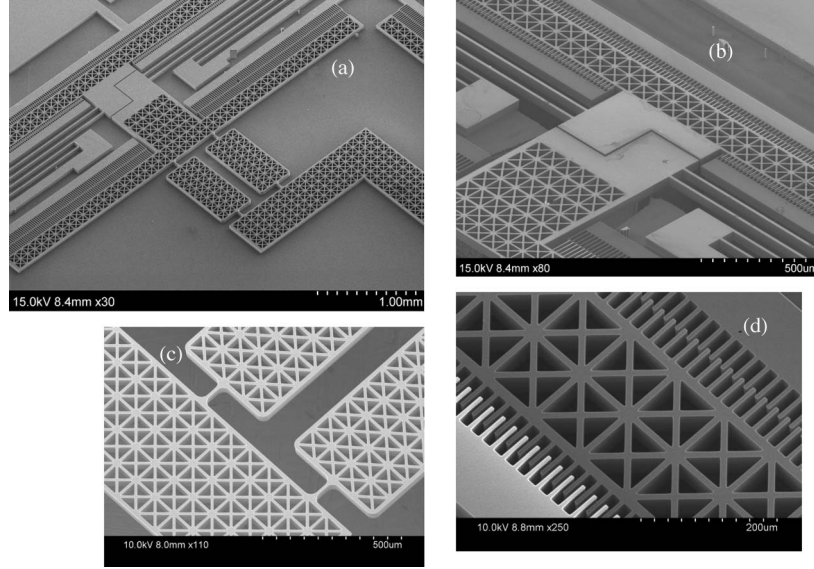
Fig. 6.   SEM pictures for micropositioning XY stage. (a) Overall, structure. (b) Isolation between actuation and sensing comb drives. (c) Hinges. (d) Differential comb drives for sensing.
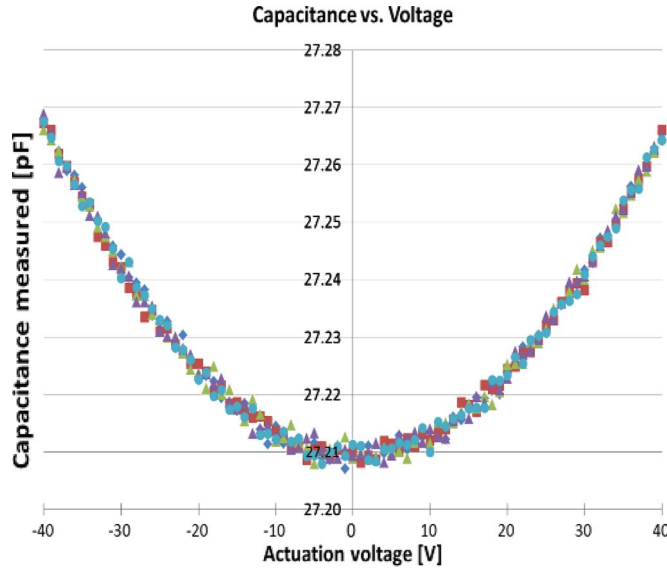

Fig. 7.   Sensing comb calibration with LCR meter.

Fig. 8.   Voltage-displacement characteristics for the two axes.

Fig. 9 shows the circuit schematic for displacement measurement circuit with the sensing combs connected to the MS3110 IC. The IC is powered by a battery cell to reduce the effects of the line noise on the measurements. It is operated in a differential capacitance mode (CS2-CS1) with CS2 connected to sensing comb SEN1 and CS1 connected to sensing comb SEN2 with a tuneable capacitor connected in parallel. The tuneable capacitor is used to balance the difference between the two sensing comb drives so that the overall capacitance is in proper range (0.5 pF∼10 pF) for the sensor, as shown in Fig. 9.

Fig. 10(a) shows the capacitance readings at the sensing combs of the X axis of the stage for different voltages at the actuation comb. The results from the Y-axis follow a similar behavior. The information from displacement test in Fig. 8 is integrated with capacitive measurement test to produce the capacitance-displacement characteristics for the axis, given in
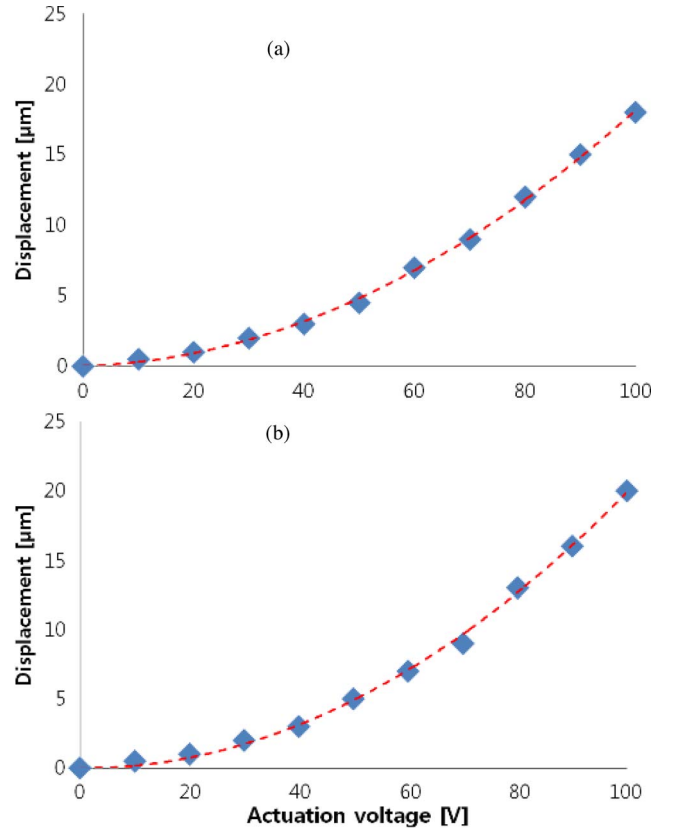
Fig. 10(b). For the entire displacement range, it can be observed that the characteristics are linear as one would expect, producing a sensitivity of 0.0136 pF/micrometer for x-axis and 0.0130 pF/micrometer for y-axis. With a conversion gain of 5.5347 volts/pF and a 16 bit D/A converter, one can expect a displacement resolution of 1.01 nm for x-axis and 1.06 nm for y-axis with this system. Note that the experimental values for sensitivity of the x and y-axis combs are only 45% and
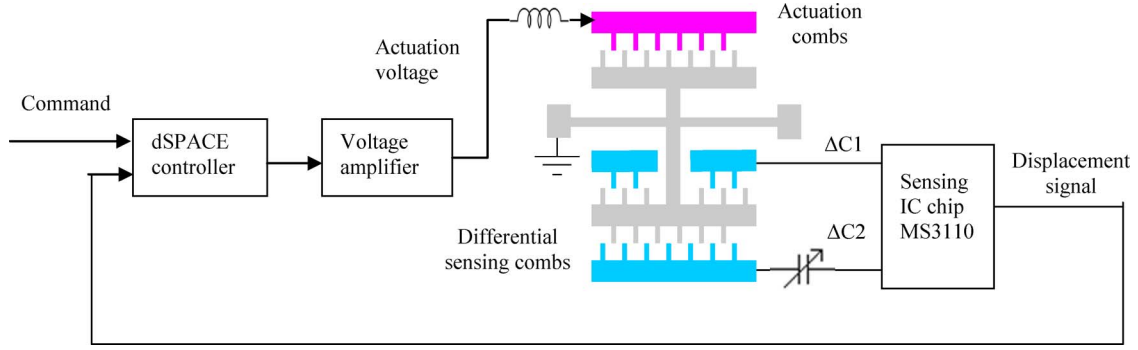
Fig. 9.   Circuit diagram for the actuation and sensing needed for control implementation.
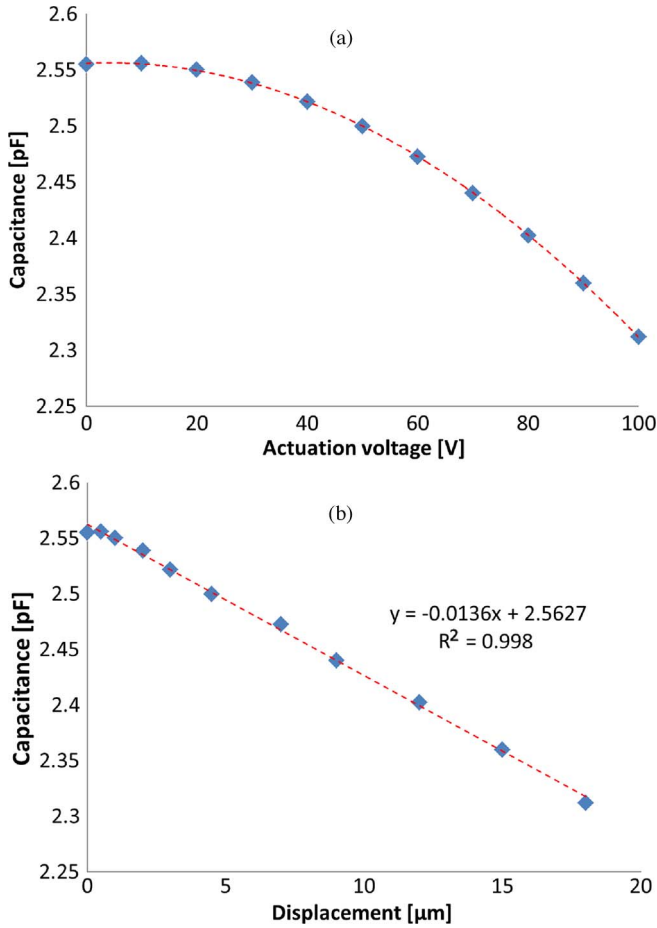

Fig. 10.   Calibration of actuation comb drives and sensing comb drives. (a) Measured capacitance when actuated. (b) Measured capacitance follows a linear relationship with displacement.
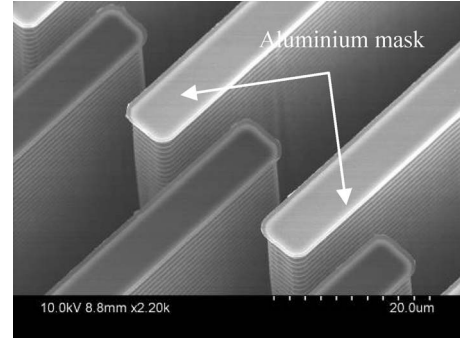

Fig. 11.   SEM image shows undercutting of comb fingers after DRIE process.

Finally, the stage is experimentally characterized for its modal frequencies. A sinusoidal waveform with frequencies swept for 1 to 1000 Hz is fed from the signal generator (WAVETEK Model 19) with gain adjusted to maximum output amplitude of 19.3 V to the comb. The amplitude of motion of the end-effector is observed on the microscope (1-micrometer resolution) of the probe station. A resonant peak is seen at around 600 Hz. This is smaller than the first dominant frequency predicted by the FEA analysis (at 1120 Hz). The discrepancy is due to fabrication imperfections, as the stiffness of the hinges and leaf springs are very sensitive to small dimensional changes in their thickness, which is very close to the fabrication resolution limitation. Also, compared to our previous reports on similar device designs [21], [22], we see a significant broadening of the peak and a smaller Q factor. This could be the result of the viscous thin-film damping in the two additional sensing combs (with large overlap between the fingers, see Fig. 6) that have been introduced in this design.

43% of theoretical value of 0.0305 pF/μm, expected from the comb design. This discrepancy is mainly caused by finger gap variation caused by undercutting during DRIE fabrication process as shown in Fig. 11. A SEM picture of the comb fingers was taken right after the DRIE process. A undercutting can be observed between the Al mask and the underneath actual silicon structure below Al mask. The actual gap for the fabricated device was measured to be 9 μm in SEM micrographs, while the designed value is 5 μm. This reduces the expected sensitivity $(\Delta C/\Delta x)$ to 0.0169 pF/μm. With this adjustment, the measured sensitivities for x-axis and y-axis are a more reasonable 80% and 77% of expected value, respectively.

IV. CONTROL SETUP AND EXPERIMENTAL RESULTS

Open-loop response results of the system shown in Fig. 12 are obtained with both step input and sinusoidal input. As the voltage increases by a fixed amount (10 V) in each step, the increment of voltage output from the measurement chip becomes larger at higher actuation voltage as shown in Fig. 12(a). This is expected since the electrostatic forces and, hence, displacement of the device are proportional to V^2. The rise time for the system for a step input is approximately 30 ms with large overshoot, and its settling time is about 150 ms. For sinusoidal command inputs $(f = 1 \text{ Hz})$, the output can be seen to the square of a sine wave.
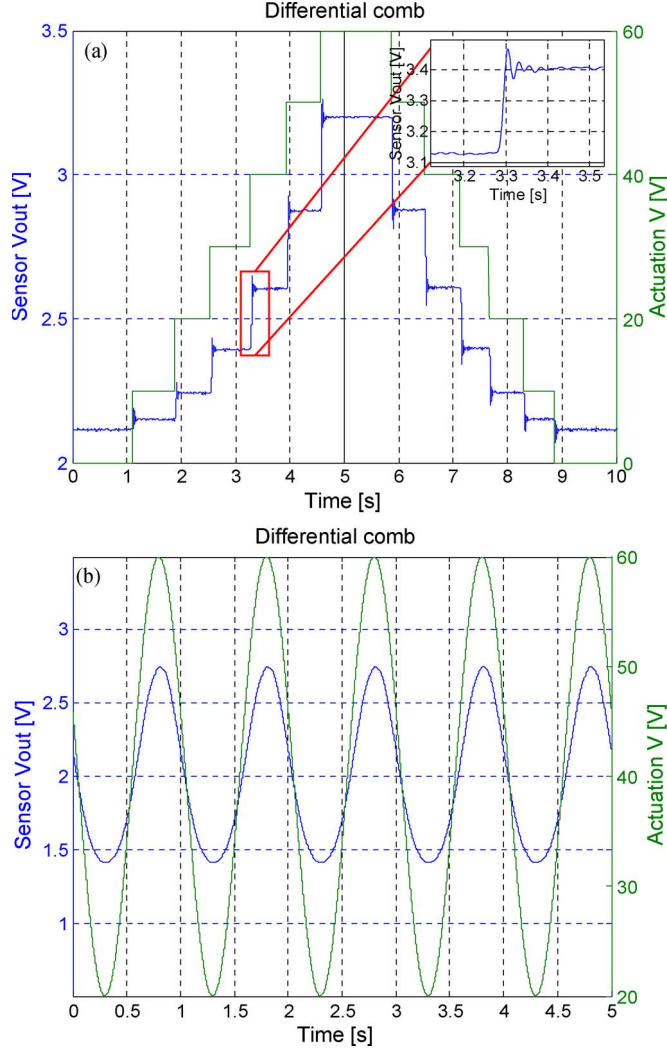
Fig. 12. Open-loop response for MEMS XY stage showing the voltage output of capacitance-to-voltage IC and the corresponding actuation voltage for (a) step input, and (b) sinusoidal input.

Fig. 13. Open-loop response for the MEMS XY stage. (a) Response for sensing comb SENS1. (b) Open-loop response for sensing comb SENS2.

As mentioned in an earlier section, the sensing on each axis consists of two sensing combs, such that when actuated, the capacitance at one comb (SENS1) increases and that at the other (SENS2) decreases. Fig. 13(a) and (b) shows the voltage signals output of capacitance-to-voltage conversion IC individually by sensing combs SENSI and SENS2, respectively, when the actuation comb is driven with a sinusoidal actuation voltage having amplitude of 20 V and an offset (bias) of 40 V. They can be seen to be 180° out of phase. The peak-to-peak change of 0.7906 V is obtained in the output voltage signal for SENS1, while that for SENS2 is 0.5082 V. This is expected since, because of the design, SENS1 has more fingers than SENS2. When used together in a differential mode, supported by the MS3110 IC, the sensitivity $(\Delta C/\Delta x)$ of the system is increased, as indicated by peak-to-peak variation of 1.3353 V in the output voltage shown in Fig. 12(b).

The main use for the sensors that have been introduced into each axis of the stage is that they can be used for feedback-control design. Fig. 14 represents the feedback control-block diagram of the system. Appropriately designed feedback laws $K(s)$ and their implementations can lead to significant im-
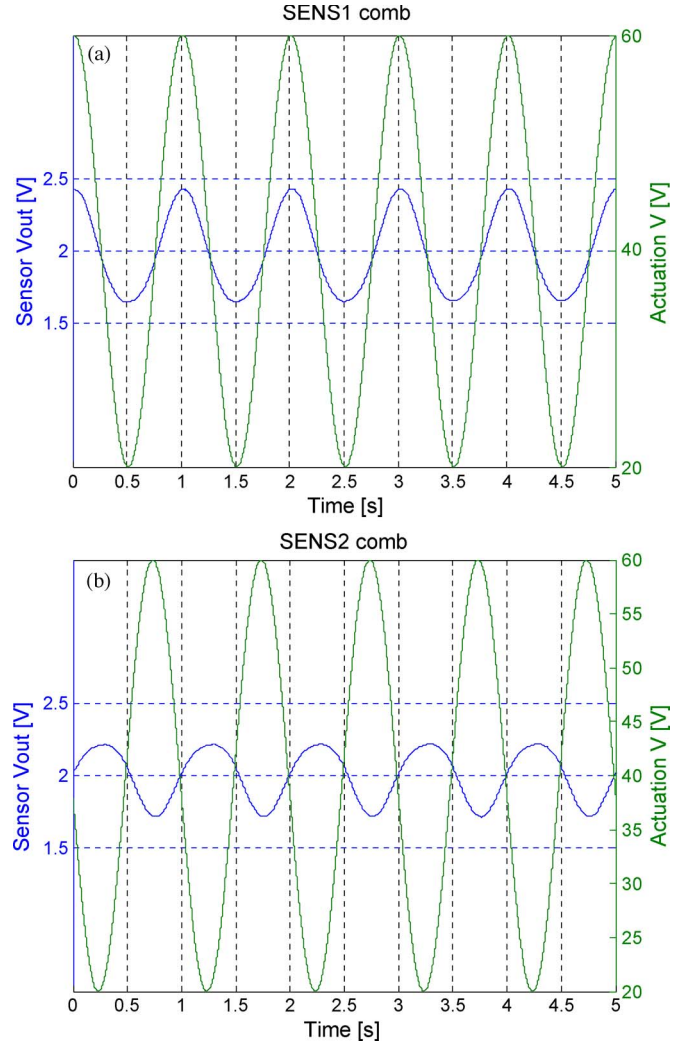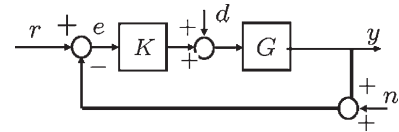

Fig. 14. Control block-diagram schematic of the closed-loop device. Here, r, u, n, d, y, and $e = r - y$ represent the tracking reference, actuator input, the sensor noise, mechanical disturbances, the stage displacement, and the error signal; and the transfer function G represents the MEMS device comprising of the actuation stage and detection stages, and the transfer function K represents the controller transfer function.

provements in the positioning bandwidth and resolution, while also enhancing the reliability of the positioning system. In this paper, these improvements are demonstrated by implementation of a PID control design. The PID control law $u(t)$ is given by $u(t) = K_p e(t) + K_i \int_0^t e(\tau)d\tau + K_D(de/dt)$, (or equivalently $K(s) = K_p + K_i s + K_D s$ where the proportional, integral, and derivative gains K_p, $K_i s$, and K_D are design parameters. We used Ziegler-Nichols method for tuning these parameters (see [27] for details). This method requires multiple experiments to determine these constants. We avoided this cumbersome experimentation procedure by determining
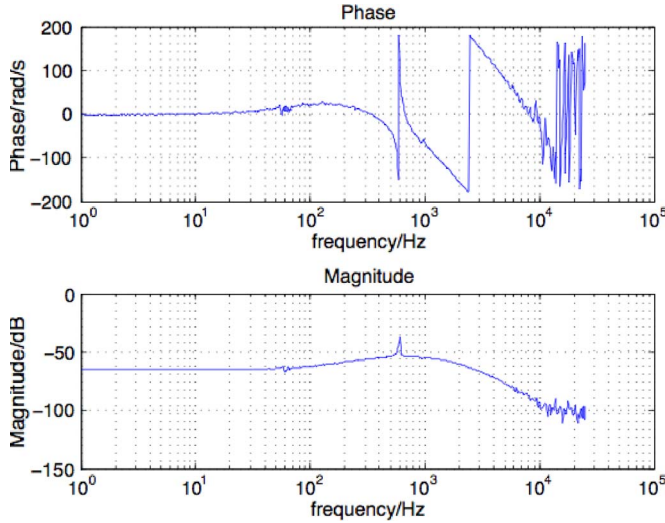
Fig. 15.   Bode plot of the dynamic model of one axis of the stage.

a model for the positioning system $G(s)$ and obtained the design parameters through numerical simulation of the Ziegler-Nichols process on the model G. To obtain a dynamic system model of the MEMS positioning stage, a sine-sweep frequency-domain identification method is applied. The main concept of this method is to excite the system through swept sinusoidal inputs over a range of frequencies, obtain the corresponding system responses, and then fit a corresponding dynamic system that has the same input-output behavior. We implemented this method using a dynamical system analyzer (DSA) which provides sinusoidal command voltage from one channel and collects the responses (stage displacement) in the other. The sweeping range is set to be 1 Hz to 25 kHz in the test. The frequency resolution is set to be 100 points per decade. The result is shown in Fig. 15. From the obtained bode plot from the above identification scheme, we fit a transfer function to the experimental frequency response data. A tenth order model is obtained which include the dynamics of the stage and the sensing system.

The PID controller that resulted from the Ziegler-Nichols method is given by: $K(s) = (1/(s/500) + 1)(100 + 300000(1/s))$. The performance of the system is well explained from the analysis of the error signal which is given by $e = r - y = Sr + Tn - GSd$, where $S = 1/(1 + GK)$ and $T = 1 - S$ represent the sensitivity and the complementary transfer functions. Thus the range of frequencies where $S(j\omega)$ is small provides a measure of the tracking bandwidth of system. Similarly, the effect of noise is attenuated at the frequencies where $T(j\omega)$ is small. Experimentally obtained sensitivity and complementary sensitivity transfer functions S and T are presented in Fig. 16(a) and (b) (from sine-sweep identification using a DSA at 10 kHz). As we can see in these two figures, the simulation and experiment matches well up to 500 Hz. The closed-loop bandwidth defined by S is around 26 Hz while that defined by T is around 32 Hz. Since the closed-loop bandwidth of T is 32 Hz, this design attenuates the noise beyond 32 Hz, while open-loop system has a larger frequency range (> 100 Hz as seen in Fig. 15) beyond which it attenuates the noise. Therefore, the closed-loop system is less sensitive to noise. In fact,

the standard deviation of the closed-loop noise output (when the input is maintained at zero) is reduced by 20% over the noise outputs from the open loop. This estimate is conservative since the open-loop system attenuates the noise at the low frequencies, even within the closed-loop bandwidth frequency range. From Fig. 15, it is evident that the open-loop system does not provide constant gain (amplification) at low frequencies, which makes it difficult to define its tracking bandwidth. Thus, in the open-loop implementation, the sensor output reading is very sensitive to the frequency content of the actuator input (even at low frequencies). This undesirable aspect is removed in the closed-loop system, which is represented by the T transfer function. The sensitivity transfer function S is small in the low-frequency range (< 27 Hz) which implies that the positioning system is insensitive to modeling uncertainties, which can include effects of disturbances, changing environmental conditions, and other modeling uncertainties. This implies that the closed-loop system is more reliable. The open-loop system has very small damping which results in it being sensitive to noise and disturbances at frequencies close to its resonance frequency.

Step and sinusoidal tracking performances are shown in Fig. 16(c) and (d), which shows the closed-loop response of the x-axis (that of the y-axis is essentially the same) to the input, with the stage operating in ambient conditions. The step response suggests a rise time of 50 ms and settling time of 100 ms. With closed-loop position regulation, under ambient conditions, the standard deviation of the feedback signal is observed to be approximately 3.8916E-4V which corresponds to 5.24 nm in terms of positioning. Fig. 16(d) show the response to a sinusoidal input ($f = 7$ Hz). The closed-loop system follows the command signal very well with tiny amplitude and phase error.

V. CONCLUSION

This paper has reported on the successful design, fabrication, and closed-loop control of a 2 DOF, translational (XY) MEMS positioning stage. The device is PKM to resolve the challenge of designing multi-axis microstage, with large displacements, low parasitic motion, and high mechanical bandwidth. Using standard photolithography and deep reactive ion etching (DRIE), the device can be fabricated on a SOI wafer. The fabricated device has 20 μm movement for an actuation voltage of 100 V. The device has integrated capacitive sensing as a result of the inclusion of sensing combs into the stage design. These sensing combs produce an experimentally measured sensitivity ($\Delta C/\Delta x$) of around 0.0130 pF/μm.

The displacement sensing for the stage is accomplished by sensing the capacitance changes at the sensing combs using a capacitance-to-voltage conversion IC. The system produces voltage signal of around 0.074 V/μm (1.3363 sensor Vout/ 18 micrometer). A rudimentary PID-based closed-loop system was implemented using a commercially available embedded control platform. The closed-loop system has a bandwidth of about 30 Hz and a positioning uncertainty standard deviation of about 5 nm. The applications envisioned for this stage include imaging and mechanical characterization of micro and
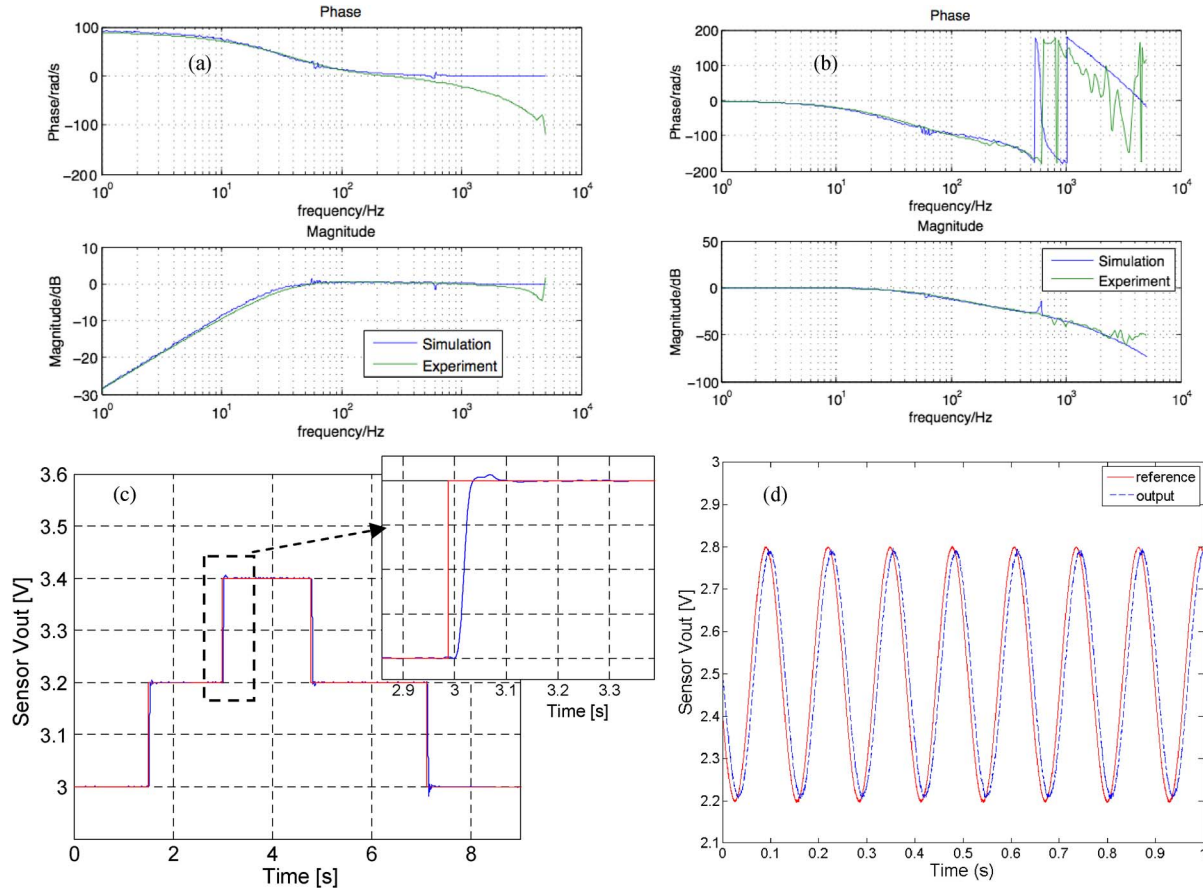
Fig. 16.   Bode plots of (a) sensitivity function S and (b) complementary sensitivity function T with the PID control design. Tracking results for a (c) step input (d) sinusoidal input of 7 Hz of the closed-loop system based on PID controller.

nanostructures such as nanowires, single cells, and microscale tissue samples. Future work will concentrate on the adaptation of this device to these applications. Additionally, closer integration of the sensing circuits with sensing structures is needed to improve the closed-loop tracking performance of the system and fully exploit the mechanical capabilities designed into the positioning stage.

REFERENCES

[1] J. Li, Q. X. Zhang, and A. Q. Liu, "Advanced fiber optical switches using deep RIE (DRIE) fabrication," *Sens. Actuators A, Phys.*, vol. 102, no. 3, pp. 286–295, Jan. 2003.

[2] Y. Sun, B. J. Nelson, D. P. Potasek, and E. A. Enikov, "Bulk microfabricated multi-axis capacitive cellular force sensor using transverse comb drives," *J. Micromech. Microeng.*, vol. 12, no. 6, pp. 832–840, Nov. 2002.

[3] Y. Sun, D. Piyabongkarn, A. Sezen, B. J. Nelson, and R. Rajamani, "A high-aspect-ratio two-axis electrostatic microactuator with extended travel range," *Sens. Actuators A, Phys.*, vol. 102, no. 1/2, pp. 49–60, Dec. 2002.

[4] P. F. Indermuehle, C. Linder, J. Brugger, V. P. Jaecklin, and N. F. de Rooij, "Design and fabrication of an overhanging xy-microactuator with integrated tip for scanning surface profiling," *Sens. Actuators A, Phys.*, vol. 43, no. 1–3, pp. 346–350, May 1994.

[5] P.-F. Indermuhle, V. P. Jaecklin, J. Brugger, C. Linder, N. F. de Rooij, and M. Binggeli, "AFM imaging with an xy-micropositioner with integrated tip," *Sens. Actuators A, Phys.*, vol. 47, no. 1–3, pp. 562–565, Mar./Apr. 1994.

[6] C.-H. Kim, H.-M. Jeong, J.-U. Jeon, and Y.-K. Kim, "Silicon micro XY-stage with a large area shuttle and no-etching holes for SPM-based data storage," *J. Microelectromech. Syst.*, vol. 12, no. 4, pp. 470–478, Aug. 2003.

[7] J.-J. Choi, H. Park, Y. K. Kyu, and U. J. Jong, "Electromagnetic micro x–y stage with very thick Cu coil for probe-based mass data storage device," in *Proc. SPIE—Int. Soc. Opt. Eng*, 2001, vol. 4334, pp. 363–371.

[8] Y. Lu, C. K. Pang, J. Chen, H. Zhu, J. P. Yang, J. Q. Mou, G. X. Guo, B. M. Chen, and T. H. Lee, "Design, fabrication and control of a micro X–Y stage with large ultra-thin film recoding media platform," in *Proc. 2005 IEEE/ASME Int. Conf. AIM*, 2005, pp. 19–24.

[9] M. Epitaux, J.-M. Verdeil, Y. Petremand, W. Noell, and N. F. de Rooij, "Micro-machined XY stage for fiber optics module alignment," in *Proc. IEEE Conf. Opt. Fiber Commun.*, Anaheim, CA, 2005, pp. 131–133.

[10] C.-H. Kim and Y.-K. Kim, "Integration of a micro lens on a micro XY-stage," in *Proc. SPIE—Int. Soc. Opt. Eng*, 1999, vol. 3892, pp. 109–117.

[11] K. Takahashi, H. N. Kwon, K. Saruta, M. Mita, H. Fujita, and H. Toshiyoshi, "A two-dimensional $-\theta$ micro optical lens scanner with electrostatic comb-drive XY-stage," *IEICE Electron. Exp.*, vol. 2, no. 21, pp. 542–547, Nov. 2005.

[12] K. Takahashi, M. Mita, H. Fujita, and H. Toshiyoshi, "A high fillfactor comb-driven XY-stage with topological layer switch architecture," *IEICE Electron. Exp.*, vol. 3, no. 9, pp. 197–202, May 2006.

[13] V. P. Jaecklin, C. Linder, N. F. de Rooij, J. M. Moret, R. Bischof, and F. Rudolf, "Novel polysilicon comb actuators for xy-stages," in *Proc IEEE Micro Electro Mech. Syst. Workshop*, 1992, pp. 147–149.

[14] C. S. B. Lee, S. Han, and N. C. MacDonald, "Single crystal silicon (SCS) XY-stage fabricated by DRIE and IR alignment," *Proc. IEEE MEMS*, pp. 28–33, 2000.

[15] C.-H. Kim and Y.-K. Kim, "Micro XY-stage using silicon ona glass substrate," *J. Micromech. Microeng*, vol. 12, no. 2, pp. 103–107, Mar. 2002.

[16] T. Harness and R. R. A. Syms, "Characteristic modes of electrostatic comb-drive X–Y microactuators," *J. Micromech. Microeng.*, vol. 10, no. 1, pp. 7–14, Mar. 2000.

[17] Q. Yao, P. M. Ferreira, and D. Mukhopadhyay, "Development of a novel piezo-driven parallel-kinematics single crystal silicon micropositioning XY stage," in *Proc. SPIE—Int. Soc. Opt. Eng*, 2005, vol. 5836, pp. 56–66.

[18] Q. Yao, J. Dong, and P. M. Ferreira, "Design, analysis, fabrication and testing of a parallel-kinematic micropositioning XY stage," *Int. J. Mach. Tools Manuf.*, vol. 47, no. 6, pp. 946–961, May 2007.

[19] L. Yangmin and X. Qingsong, "A novel design and analysis of a 2-DOF compliant parallel micromanipulator for nanomanipulation," *IEEE Trans. Autom. Sci. Eng.*, vol. 3, no. 3, pp. 248–253, Jul. 2006.

[20] J. Dong and P. M. Ferreira, "Electrostatically actuated cantilever with SOI-MEMS parallel kinematic XY stage," *J. Microelectromech. Syst.*, vol. 18, no. 3, pp. 641–651, Jun. 2009.

[21] J. Dong, D. Mukhopadhyay, and P. M. Ferreira, "Design, fabrication and testing of Silicon-on-Insulator (SOI) MEMS parallel kinematics XY stage," *J. Micromech. Microeng.*, vol. 17, no. 6, pp. 1154–1161, Jun. 2007.

[22] J. Dong and P. M. Ferreira, "Simultaneous actuation and displacement sensing for electrostatic drives," *J. Micromech. Microeng.*, vol. 18, no. 3, pp. 035011-1–035011-10, Mar. 2008.

[23] J. Dong, S. Salapaka, and P. Ferreira, "Robust control of a parallel kinematic nano-positioner," *ASME J. Dyn. Syst., Meas. Control*, vol. 130, no. 4, pp. 041007-1–041007-15, Jul. 2008.

[24] S. Yang and T. Saif, "Micromachined force sensors for the study of cell mechanics," *Rev. Sci. Instrum.*, vol. 76, no. 4, pp. 044301-1–044301-8, Apr. 2005.

[25] S. Yang and T. Saif, "Microfabricated force sensors and their applications in the study of cell mechanical response," *Exper. Mech.*, vol. 49, no. 1, pp. 135–151, Feb. 2009.

[26] P. Vettiger, G. Cross, M. Despont, U. Drechsler, U. Durig, B. Gotsmann, W. Haberle, W. M. A. Lantz, H. E. Rothuizen, R. Stutz, and G. K. Binnig, "The 'millipede'—Nanotechnology entering data storage," *IEEE Trans. Nanotechnol.*, vol. 1, no. 1, pp. 39–55, Mar. 2002.

[27] K. J. Astrom and T. H. Hagglund, *PID Controllers: Theory, Design, and Tuning*. Research Triangle Park, NC: ISA, 1995.

Bonjin Koo received the Bachelor's degree in mechanical engineering from Purdue University, West Lafayette, IN, in 2008. He is currently working toward the Master's and Doctoral degrees in the Department of Mechanical Science and Engineering, University of Illinois at Urbana-Champaign, Urbana.

His research interests include micro/nanomanufacturing and system control in micro/nanoscale.

Xuemeng Zhang received the B.S. degree in instrumentation and controls from Tsinghua University, Beijing, China, in 2008, and the M.S. degrees in mechanical engineering and mathematics, from the University of Illinois at Urbana-Champaign, Urbana, in 2011.

He is currently working on warehouse automation and robotics at Elettric 80, Inc., Skokie, IL.

Jingyan Dong received the B.S. degree in automatic control from the University of Science and Technology of China, Hefei, China, in 1998, the M.S. degree from the Chinese Academy of Sciences, Beijing, China, in 2001, and the Ph.D. degree in mechanical engineering from the University of Illinois at Urbana-Champaign, Urbana, in 2006.

He is currently an Assistant Professor in the Department of Industrial and Systems Engineering at the North Carolina State University, Raleigh, where he has been a Faculty Member since 2008. From 2006 to 2008, he was a Postdoctoral Researcher with the Center for Chemical-Electrical-Mechanical 657 Manufacturing Systems (Nano-CEMMS) at the University of Illinois. His research interests include micro/nanomanufacturing, multidimensional scale mechatronics, and manufacturing systems.

Srinivasa M. Salapaka was born in Andhra Pradesh, India, in 1973. He received the B.Tech. degree in mechanical engineering from the Indian Institute of Technology, Chennai, India, in 1995, and the M.S. and Ph.D. degrees in mechanical engineering from the University of California, Santa Barbara, in 1997 and 2002, respectively.
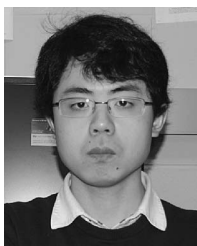
From 2002 to 2004, he was a Postdoctoral Associate in the Laboratory for Information and Decision Systems, Massachusetts Institute of Technology, Cambridge. Since 2004, he has been a Faculty Member in the Department of Mechanical Science and Engineering, University of Illinois at Urbana-Champaign, Urbana. His areas of current research interest include controls for nanotechnology, combinatorial resource allocation, and numerical analysis.

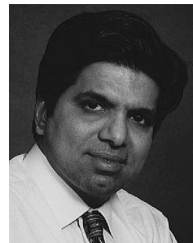Dr. Salapaka received a National Science Foundation CAREER Award in 2005.

Placid M. Ferreira received the B.E. (Mechanical) degree from the University of Bombay, Mumbai, India, in 1980, the M.Tech (Mechanical) degree from the Indian Institute of Technology Bombay, India, 1982, and the Ph.D. degree in industrial engineering from Purdue University, West Lafayette, IN, in 1987.

He is the Head and the Grayce Wicall Gauthier Professor of Mechanical Science and Engineering at the University of Illinois at Urbana-Champaign, Urbana. From 2003 to 2009, he was the Director of the Center for Chemical-Electrical-Mechanical Manufacturing Systems (Nano-CEMMS), an NSF-sponsored Nanoscale Science and Engineering Center. He has been on the mechanical engineering faculty at the University of Illinois, since 1987, serving as the Associate Head for graduate programs and research from 1999 to 2002. His research interests include nanomanufacturing, precision engineering, and machine tools.

Dr. Ferreira received an NSF Presidential Young Investigator Award in 1990, the Society of Manufacturing Engineers Outstanding Young Investigator Award in 1991, and the University of Illinois University Scholar Award in 1994. He became a Fellow of the Society of Manufacturing Engineers in 2011.